



# Electrocatalytic methanol oxidation over Cu, Ni and bimetallic Cu-Ni nanoparticles supported on graphitic carbon nitride



Izabela S. Pieta<sup>a,\*</sup>, Anuj Rathi<sup>b</sup>, Piotr Pieta<sup>a</sup>, Robert Nowakowski<sup>a</sup>, Marcin Hołdynski<sup>a</sup>, Marcin Pisarek<sup>a</sup>, Agnieszka Kaminska<sup>a</sup>, Manoj B. Gawande<sup>b</sup>, Radek Zboril<sup>b</sup>

<sup>a</sup> Institute of Physical Chemistry Polish Academy of Sciences, 01-224, Warsaw, Poland

<sup>b</sup> Regional Centre of Advanced Technologies and Materials, Faculty of Science, Palacky University, Šlechtitelů 27, 783 71, Olomouc, Czech Republic

## ARTICLE INFO

### Keywords:

Electrocatalysis  
Methanol electrooxidation  
Ni catalyst  
g-C<sub>3</sub>N<sub>4</sub>  
Ni/C<sub>3</sub>N<sub>4</sub>  
Advanced nanomaterials

## ABSTRACT

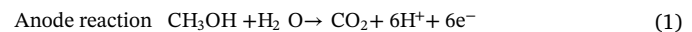
Ni, Cu and Cu–Ni nanostructures have been fabricated and homogeneously embedded on ultrathin two-dimensional (2D) carbon nitride (g-C<sub>3</sub>N<sub>4</sub>), and the surface morphology and composition of the resulting hybrid nanostructures were studied by XRD, TEM, HRTEM-elemental mapping, Raman spectroscopy and XPS. The new hierarchical hetero-structures dropcasted on GC anodes have been visualised by SEM and their catalytic performance have been examined in methanol electrooxidation reaction (MOR) under alkaline conditions. Nanosized Ni particles dispersed finely over g-C<sub>3</sub>N<sub>4</sub> are very active electrocatalysts with MOR onset at potential 0.35 V and charge transfer resistance 0.12 kΩ. The stability of modified GC electrodes, examined under chronoamperometric conditions showed that for electrode loading with 4% (wt. %) of NiO the stable current density ca. 36 A g<sup>-1</sup> (12 A cm<sup>-2</sup>) was obtained during whole experiment (up to 160 min). For all catalyst studied the current density obtained during MOR reaction was enhanced when electrode was illuminated by UV light  $\lambda \sim 400$  nm, and the highest value were obtained for 4% Ni/CN catalyst ca. 127 A g<sup>-1</sup> (22 A cm<sup>-2</sup>). The Cu incorporation in the hybrid material evoke loss of activity mostly due to Cu<sup>+</sup> irreversible reduction/oxidation to Cu<sup>0</sup> and Cu<sup>2+</sup>, CuO segregation and influencing electron transfer process which results in the increasing in the redox potential. These results represent an important step towards light-enhanced electro-reactive systems and sensors in which heterojunction formation can facilitate electron-hole separation and enable more efficient energy transfer.

## 1. Introduction

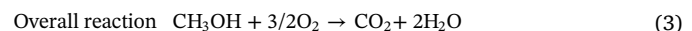
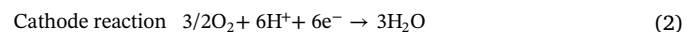
Modern energy and transport systems are mainly based on fossil fuels, with oil as the primary fuel, and so cannot be considered sustainable [1–4]. Considerable efforts have been made to diversify energy supplies and develop cleaner and more universal fuels [1,4]. Several researchers have highlighted the advantages of biomass-derived fuels such as biogas, bio-methanol, and bioethanol, as alternatives [5]. These can be used as feedstocks in various chemical processes to valuable products, with applications including synthetic fuels and in fine chemical synthesis, among others [6,7].

Methanol is commercially prepared from synthesis gas and used to produce many fine chemicals [8–10]. As methanol-gasoline/methanol-diesel blends is used for internal combustion (IC) engines [11]. Moreover, it is an economical and readily available fuel that can be obtained from bio-resources, is suitable for fuel cell applications, and can be distributed using existing infrastructure [12–14]. The catalytic

oxidation of methanol is a promising technology with potential applications in direct methanol fuel cells (DMFC) [15,16]. As DMFC fuel methanol undergoes oxidation on anode catalyst in the presence of H<sub>2</sub>O to produce CO<sub>2</sub>, H<sup>+</sup> and e<sup>-</sup> according to Eq. (1).



Electrons (e<sup>-</sup>) are transporting through circuit and protons (H<sup>+</sup>) diffuse from anode through membrane to reduce oxygen on cathode catalyst (2).



DMFCs have been studied extensively because of their potential applications in portable electronic devices and non-petroleum-fueled vehicles [17–19]. However, efficient, stable, durable, and inexpensive catalysts are needed to make methanol an economically attractive

\* Corresponding author.

E-mail address: [ipieta@ichf.edu.pl](mailto:ipieta@ichf.edu.pl) (I.S. Pieta).

DMFC fuel. The overall efficiency of DMFC depends on the kinetics of the anodic methanol oxidation reaction (MOR) [20,21]. Catalysts using Pt-based anodes have been studied extensively, but have several inherent drawbacks including high costs, the limited reserves of precious metals, and high susceptibility to poisoning by CO and HCO species [22,23]. It was found that for Pt solution in acidic medium at potentials above approx. 0.5 V [vs. NHE], there is a steady loss of adsorbed CO from the Pt surface and above 0.7 V, the surface is almost free of adsorbed CO. However in an alkaline medium, the onset potential of the anode reaction should be lower than 0.4 V [vs. NHE], what is the standard oxygen reduction potential in the alkaline medium. In addition, the Pt-based anode performance is inadequate for practical applications because of the slow kinetics of the MOR and the oxygen reduction reaction (ORR) on current noble metal catalysts [15,17]. To overcome these problems, several groups have sought to develop new classes of catalysts that offer higher MOR rates and are less costly because they are not based on precious metals (the usage of Pt in current catalysts can be as high as 6 mg cm<sup>-2</sup>) [15,17,19]. Various other precious and transition metals have been combined with Pt to form binary, ternary, and more complex alloys for DMFC anodes, such as Au, Rh, Pd, Sn, Re, Ni, Ru-Co etc. [15,17,19,23–27]. In addition, several metal/semiconductor hybrid materials i.e. Pt–CuInS<sub>2</sub>, CdSe–Au nanoparticles (NPs), CdS–Au NPs, Pt–MWCN have been evaluated for use in anodes because of their potential for improved activity and greater reaction stability [28–30].

An alternative way to enhance the electrocatalytic activity of DMFC is to use an anode made from a transition metal/precious metal alloy. Among the transition metals that have been used for this purpose, Co, Ni, Mn, Ce, Fe and Cu are the most popular and in particular, Ni and Cu nanoparticles have attracted considerable attention due to their low cost and proven activity in various processes including reforming, decomposition, partial oxidation, and hydrogenation [2,9,15,17,22,31–33]. Their unique electronic properties also make them very promising materials for use in superconductors, electronic, optical, mechanical devices, sensors, and recording media [15]. However there are some constraints prevent utilization the transition metal-based anodes in the DMFCs, i.e. the too high onset potential for MOR and regulations for wasted NiO catalysts.

Ni-based electrodes are known for good performance for MOR, and the electrochemical MOR over Ni(II) and Ni(III) species has been explained for NiO electrodeposited on multiwalled carbon nanotubes (NiO/MWCNT) [34,35]. Moreover, it was shown that uniformly coated graphitic phase carbon nitride (GCN) on NiO nanosheets arrays under visible irradiation could effectively suppress the charge recombination of the GCN, and photogenerated holes were effectively transferred to conductive substrates through NiO nanosheet arrays [36].

For Cu-based electrocatalysts, a lower affinity for carbon monoxide (CO) than that of the Ru, Rh, Pd or Pt was demonstrated and Cu-related nanostructured materials have been reported as suitable electrocatalysts for DMFC in alkaline media [2]. Cu<sub>2</sub>O nanostructures have also been shown as a good candidate for facet-dependent photocatalytic studies because of the ease of fabrication of different Cu<sub>2</sub>O crystals shapes and facets [37]. For Cu<sub>2</sub>O/g-C<sub>3</sub>N<sub>4</sub>, p-n heterojunctions can be formed, consequently suppressing e–h interaction and favoring efficient charge carrier separation; however the formation mechanism of Cu<sub>2</sub>O nanoparticles (NPs) on g-C<sub>3</sub>N<sub>4</sub> is still unclear. Cu nanostructures prepared by the electrochemical corrosion of a Cu electrode or by electrodeposition of Cu NPs onto Cu electrodes can promote the enhancement of the electrode activity due to an increase of the effective surface area of the electrode; however, Cu NPs were reported as not stable for photocatalytic reactions, as Cu<sup>+</sup> is easy to reduce/oxidize to Cu<sup>0</sup> and Cu<sup>2+</sup> [2,38]. The properties of these materials as well as their performance can be further increased by NPs shape and anode morphology tuning to increase the anode's adsorption capacity [15,17,19,21,23,24].

Hence, the NPs crystal structure is an important factor in the enhancement of the electrode activity toward MOR, and there are a

variety of structures that have been synthesized, including nanotubes, nanofibers, nanocubes, nanoflakes, nanosheet based microspheres, and nanospheres, and can be tuned to suit particular applications [26,39,40]. Despite their promise, these materials have insufficient electrical conductivity for use in fuel cell anodes. This problem could potentially be overcome by tuning the nanostructures' sizes, morphology, and distribution, and by supporting them on a carbon-based material such as carbon black, carbon nanotubes, or 2D sheets, graphitic carbon nitride (g-C<sub>3</sub>N<sub>4</sub>), boron nitride (BN), silicene, transition metal oxides, germanene, borophene, and atomically thin 2D perovskites [41,42]. Importantly, integrating a 2D material with NPs, especially with plasmonic metal, i.e. Cu, can (i) enhance light absorption through the plasmonic effect of the metal component and then channel the absorbed light energy to the 2D material, and (ii) can improve conductivity of the hybrid nanostructures via plasmon induced “hot electrons” [43].

Among 2D materials, graphitic carbon nitride (g-C<sub>3</sub>N<sub>4</sub>) is a typical graphite-like material consisting of stacked 2D sheets of ordered tri-s-triazine subunits connected via planar tertiary amino groups. It can be regarded as an N-substituted graphite framework with a very high level of nitrogen doping, consisting of  $\pi$ -conjugated graphitic planes made up from sp<sup>2</sup>-hybridized carbon and nitrogen atoms [44–47]. Nitrogen is usually described as an n-type carbon dopant in such contexts [41,46,48]. This material has attracted substantial attention as a graphite analog with unique electronic and optical properties; it has potential applications in optoelectronic conversion, hydrocarbon oxidation, fuel cells and sensors [44,47]. Doping g-C<sub>3</sub>N<sub>4</sub> with a nanostructured conductive material could potentially produce stable and active anode materials via the interactions between the two components.

Here we report stable, inexpensive, and active anode materials consisting of Cu, Ni, and Ni–Cu nanostructures on ultrathin g-C<sub>3</sub>N<sub>4</sub> nanosheets. These materials can be prepared by a one-pot hydrothermal synthesis, as shown schematically for Cu–Ni/g-C<sub>3</sub>N<sub>4</sub> in Fig. 1. This procedure results in nanosize hierarchical metal heterostructures (Cu, Ni and Cu–Ni) uniformly embedded in ultrathin two-dimensional (2D) g-C<sub>3</sub>N<sub>4</sub>, yielding new hybrid materials with improved MOR performance under visible light irradiation. The MOR catalytic activity of the resulting Cu-, Ni-, and Cu–Ni/g-C<sub>3</sub>N<sub>4</sub> hybrid composites is up to 2.7-fold higher under visible light illumination in alkaline media than under conventional dark conditions, producing oxidation peaks with maxima at a potential of 0.56 V. The introduction of plasmonic metal, Cu in 1:1 ratio doesn't result in increased light adsorption and conductivity, but the photocatalytic reduction/oxidation of Cu<sup>+</sup> have been partially avoided indicating more stable response in photo-electrocatalytic activity with time. These results suggest that such finely tuned hierarchical nanostructures could be useful in DMFC and other electrochemical systems, leading to many potential applications in clean energy conversion and sensors.

## 2. Materials and methods

### 2.1. Preparation of nanostructured composites

Two-dimensional (2D) carbon nitride g-C<sub>3</sub>N<sub>4</sub> nanosheets were synthesized by thermal polymerization as described in the literature [14,49]. Typically, 10 g of urea (> 97% Sigma-Aldrich) was ground in a mortar and then dissolved in 15  $\mu$ L water (Milipore, ultrapure). The pH of the resulting solution was then adjusted to 4–5.5, after which it was dried at 60 °C for 12 h and transferred to an alumina crucible with a lid. The precursor was heated to 550 °C in a muffle furnace at a heating rate of 5 °C min<sup>-1</sup>, and maintained at 550 °C for 2 h to yield ultrathin g-C<sub>3</sub>N<sub>4</sub> nanosheets.

The following hybrid nanocatalysts were evaluated in this work: 4Ni/g-C<sub>3</sub>N<sub>4</sub>, 4Cu/g-C<sub>3</sub>N<sub>4</sub>, 2Cu–2Ni/g-C<sub>3</sub>N<sub>4</sub>, abbreviated as Ni/CN, Cu/CN, and Cu–Ni/CN respectively. The metal loading in these systems is

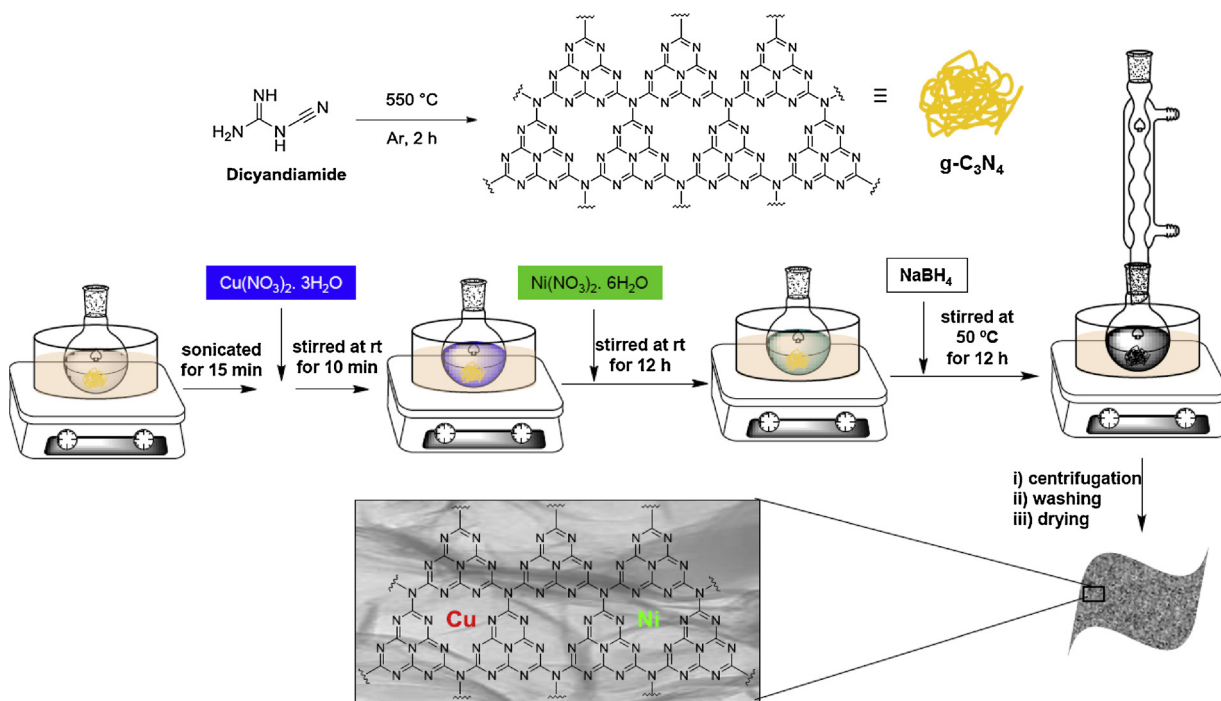


Fig. 1. TEM Synthesis of nanocatalysts.

expressed in (wt%). The nanocomposites were obtained by a simple co-precipitation method described below. Typically 0.5 g  $\text{g-C}_3\text{N}_4$  was dispersed in 175 mL water and stirred for 10 min, then an aqueous solution of  $\text{Cu}(\text{NO}_3)_2 \cdot 3\text{H}_2\text{O}$  (200 mg in 20 mL water), or  $\text{Ni}(\text{NO}_3)_2 \cdot 6\text{H}_2\text{O}$  (248 mg in 20 mL water) or both solutions were added and the reaction mixture was stirred for 18 h at room temperature. After 18 h, 1 g of sodium borohydride was added in one portion with constant stirring and the reaction was stirred for another 16 h at 50 °C before being allowed to cool to room temperature. The catalyst was collected by centrifugation, washed with methanol (30 mL × 4), and dried under reduced pressure at 60 °C.

## 2.2. Characterization

X-ray diffraction patterns (XRD) were collected using a D5000 powder diffractometer (Bruker AXS) equipped with a LynxEye strip detector providing good resolution and quick data collection.  $\text{Cu K}\alpha$  radiation was used with an X-ray tube operating at 40 kV and 40 mA. Measurements were performed using samples of around 50 mg, which were spread over a thin porous sintered glass disc and mounted vertically on the stainless steel heating block of our vacuum-proof XRD camera. The environmental camera has a cavity volume of 150 ml with a removable cap incorporating an X-ray window. The cap was secured with 12.5 mm of self-adhesive Kapton foil, and the camera was connected to the gas line via Swagelok vacuum fittings and flexible stainless steel tubing, enabling XRD measurements in the Bragg–Brentano geometry [50].

Microscopic images were obtained using a HRTEM TITAN 60–300 instrument with an X-FEG-type emission gun operating at 80 kV. This microscope is equipped with a Cs image corrector and a STEM high-angle annular dark-field detector (HAADF); its point resolution is 0.06 nm in TEM mode. Elemental mappings were obtained by STEM-energy dispersive X-ray spectroscopy (EDS) with an acquisition time of 20 min. For HRTEM analysis, the powder samples were dispersed in ethanol and sonicated for 5 min. One drop of the resulting solution was then placed on a copper grid with a holey carbon film, after which the sample was dried at room temperature.

The chemical composition of the hybrid nanocatalysts was

measured by XPS spectroscopy using a Microlab 350 instrument (Thermo Electron). XPS spectra were acquired using  $\text{AlK}\alpha$  ( $\hbar\nu = 1486.6$  eV) radiation. Survey spectra and high resolution spectra were recorded using pass energies of 100 and 40 eV, and the XPS signal intensity was determined using linear or Shirley background subtraction. Peaks were fitted using an asymmetric Gaussian/Lorentzian mixed function, and the measured binding energies were corrected based on the C1s energy at 285.0 eV.

A Nicolet iS50 FT-IR spectrometer with a built-in all reflective, mid- and far-IR diamond attenuated total reflectance (ATR) module was used to record the IR spectra of as-prepared nanocomposites. Typically, 100 scans were collected at a resolution of  $1\text{ cm}^{-1}$ .

Raman and SERS Spectroscopy measurements were performed with a Renishaw inVia Raman system equipped with a 785 nm diode laser. The laser beam was passed through a line filter and focused on a sample mounted on an X-Y-Z translation stage with a  $20\times$  microscope objective,  $\text{NA} = 0.25$ . The beam diameter was approximately 5  $\mu\text{m}$ , and the laser power at the sample was 5 mW or less. The microscope was fitted with a grating having 1200 grooves per mm, cutoff optical filters, and a  $1024 \times 256$  pixel Peltier-cooled RenCam CCD detector that allowed the Stokes part of the Raman spectra to be acquired with a spectral resolution of  $5\text{--}6\text{ cm}^{-1}$  and a wavenumber accuracy of  $2\text{ cm}^{-1}$ . The experiments were performed under ambient conditions using a back-scattering geometry. The time required to acquire a single SERS spectrum was 20 s, and the laser power at the sample was around 2 mW.

SEM images were obtained using the field-emission scanning electron microscope (FE-SEM) FEI Nova NanoSEM 450 Series under high vacuum (ca. 10–6 mbar). The sample powders were deposited onto the typical SEM specimen stub for precise positioning under the electron column for imaging. SEM images were collected using the Through Lens Detector (TLD) of secondary electrons at primary beam energy of 10 keV and 4.8 mm working distance from the pole piece. All images were obtained at long scan acquisition time (20  $\mu\text{s}$ ) of typically 30 s per image after choosing the inspection region.

### 2.3. Catalyst film deposition on the GC electrode surface for electrochemical characterization

Modified GC electrodes were prepared by sonicating 1.83 mg of the appropriate powdered catalyst in 0.76 mL of Milli-Q ultrapure water containing 7.6  $\mu$ L of Nafion for 0.5 h to prepare a good dispersion of the chosen catalyst. A 10  $\mu$ L aliquot of this suspension was then drop casted onto the GC electrode surface, after which the electrode was dried under ambient conditions for 12 h.

### 2.4. Electrocatalytic methanol oxidation

Electrochemical experiments including cyclic voltammetry (CV), electrochemical impedance spectroscopy (EIS), and chronamperometry were performed with a VSP electrochemistry system supplied by BioLogic Science Instruments and controlled using the EC-Lab software package developed by the same company. All experiments were performed in a 1 M NaOH electrolyte solution under an argon atmosphere at ambient temperature,  $(20 \pm 1)^\circ\text{C}$ . Measurements were performed using a three-electrode electrochemical cell with a 4-mm in diameter glassy carbon (GC) working electrode, a Pt wire as the counter electrode, and an Ag/AgCl/KCl<sub>sat</sub> reference electrode.

CV measurements were conducted within the potential range of 0.00–0.80 V vs. Ag/AgCl at a scan rate of 50 mV s<sup>-1</sup>.

Before the EIS measurements, an equilibrium state was established by applying a potential of 0.60 V for 30 s. After that time, the current had reached equilibrium, and EIS was performed with a voltage amplitude of 5 mV and a frequency range of 100 kHz–10 mHz.

The current densities are represented as A g<sup>-1</sup>, taking into account the catalyst active phase loading onto support CN (4Ni/CN, 4Cu/CN, 2Cu-2Ni/CN, wt %). The results for bare CN (0.0238 mg dropcasted onto a GC electrode 4 mm in diameter; 0.1256 cm<sup>2</sup>) are given in SI.

## 3. Results and discussion

### 3.1. Nanostructured composites characterization

The as-prepared g-C<sub>3</sub>N<sub>4</sub> support (henceforth referred to as CN) and the Cu/g-C<sub>3</sub>N<sub>4</sub> (henceforth Cu/CN), Ni/g-C<sub>3</sub>N<sub>4</sub> (Ni/CN) and Cu-Ni/g-C<sub>3</sub>N<sub>4</sub> (Cu-Ni/CN) catalysts were characterized using conventional physicochemical and electrochemical techniques. The XRD patterns of the CN, Cu/CN, Ni/CN and Cu-Ni/CN nanocomposites are presented in Fig. 2. A strong peak at  $2\theta = 27.4^\circ$  was observed for all samples, indicating the stacking of  $\pi$ -conjugated layers, and was indexed for graphitic materials as the (0 0 2) peak [14,51]. The sizes and interlayer distances of the corresponding nanosheets were calculated to be in the

range 1.1–1.5 nm and 0.32–0.35 nm, respectively. All the prepared nanocomposites exhibited broad features in the low  $2\theta$  region due to their fine nanostructures. The assignment of the corresponding XRD peaks for CuO, NiO, and Cu<sub>x</sub>Ni<sub>(1-x)</sub> are given in Table S1, Supporting Information. The clear signal from CuO and NiO phases were obtained for Cu/CN and Cu-Ni/CN catalyst, indicating partial particles segregation and agglomeration. In the case Ni/CN the NiO phases stayed beyond XRD detection, suggesting a fine (nm) distribution of the transition metals on the CN support.

The catalysts' structural morphology and elemental distributions were investigated using TEM and elemental mapping (Figs. 3 and 4). The TEM images (Fig. 3) show that the g-C<sub>3</sub>N<sub>4</sub> matrix adopted a fine sheet-like morphology differing markedly from that seen for the Cu/CN, Ni/CN, and Cu-Ni/CN catalysts. The TEM images of Cu/CN showed agglomerated Cu and CuO nanoparticles on g-C<sub>3</sub>N<sub>4</sub>, whereas Ni/CN exhibited a unique sponge-like morphology with a network of small "branches". The elemental mapping (Fig. 4) demonstrated the presence of well dispersed, small Cu and Ni. Because of their small sizes and weak contrast, the individual Cu- and Ni-based nanoparticles on the g-C<sub>3</sub>N<sub>4</sub> matrix could not be distinguished in the TEM images.

XPS measurements were performed to determine the chemical state of the elements in the studied samples. Figs. 5 and S1 and S2 present the full survey spectra of CN and the Cu- and/or Ni-modified nanocomposites, showing the signals for C, N, O, Cu and Ni. The as-prepared CN was highly pure, consisting mainly of the elements C, N, and O. The atomic ratio of C to N at the surface of the CN samples was around 0.73, which is close to the ideal value of 0.75 for g-C<sub>3</sub>N<sub>4</sub> [52,53]. The C1s spectra of CN shown in Fig. S2 feature four peaks at binding energies of 284.6, 285.7, 287.7, and 288.5 eV. The standard line at 284.6 eV was assigned to adventitious carbon species, while the peaks at 285.7, 287.7 and 288.5 eV were assigned to sp<sup>3</sup>-hybridized tertiary carbon centers in C-(N)<sub>3</sub> units (285.7 eV), N=C-N and C=O species (287.7 eV), and N-C=O and C=O groups (288.5 eV). [54,55] The N1s region, shown in Fig. S2, is commonly examined to confirm the formation of the layered g-C<sub>3</sub>N<sub>4</sub> structure [55]. The N1s region of the XPS spectrum of pure CN contains three peaks, which can be ascribed to C=N=C (398.5 eV), tertiary nitrogen centers in N-(C)<sub>3</sub> units (399.8 eV), and N-H groups (400.7 eV). [14,52,53] The O 1s region (see Fig. S2) contains peaks assigned to C=O (529.5 eV), C=O (532 eV), and H<sub>2</sub>O adsorbed on the nanocomposite surface (536.3 eV). [53] The XPS spectra of the Cu- and/or Ni-modified materials, (spectra survey SI as well region C1 s, N1s) are shifted towards higher BE values, indicating that Cu and Ni NPs both probably act as electron donors to CN [53]. Moreover, the shapes of the C 1s, N 1s and O 1s peaks in the spectra of the Cu- and/or Ni-modified samples differ from those for the pure g-C<sub>3</sub>N<sub>4</sub> sample, suggesting that the identities and distributions of the most abundant surface species in these nanocomposites depend on (i) the electron donating or accepting properties of the transition metal dopant and its interactions with the 2D nanosheet-like structure of heptazine units, and (ii) the nanostructures themselves, which may favor the formation of certain species to balance the system's surface charge. The materials with the highest detected contents of C=O and N=O species were the Ni-modified nanocomposites, and samples with higher contents of Ni nanoparticles were found to also have higher contents of sp<sup>3</sup> carbon centers and N-(C)<sub>3</sub> species compared to pristine CN. Cu incorporation did not cause any obvious changes in the abundance of C-, N- and O-species over the investigated surfaces compared to the pure g-C<sub>3</sub>N<sub>4</sub> sample. Interestingly, the surface atomic C:N ratio of the Ni/CN nanocomposite was more than 30% lower than that for pristine CN (0.73). Smaller reductions were observed for Cu/CN (C/N = 0.54) and Cu-Ni/CN (C/N = 0.46). This trend is probably due to differences in the metal nanostructures' interactions with the heptazine framework of the CN support [56]. The peak intensity in the O 1s region of the XPS spectra of the Cu- and Ni-modified nanocomposites is greater than that for pristine CN, which can be related to the greater relative concentration of surface oxygenated species in the nanocomposites, especially Ni/CN. These

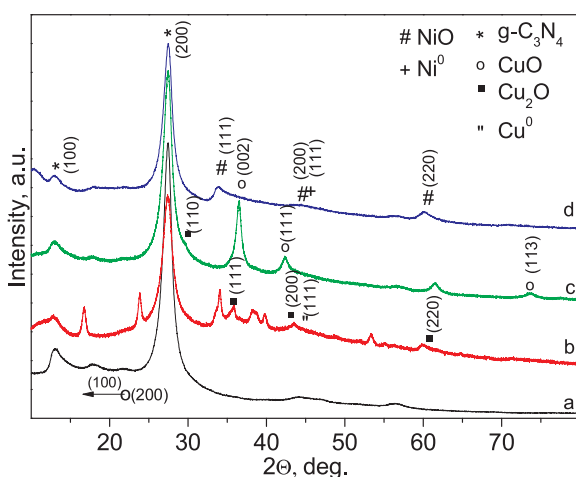


Fig. 2. XRD patterns of (a) CN, (b) CuNi/CN, (c) Cu/CN, (d) Ni/CN.

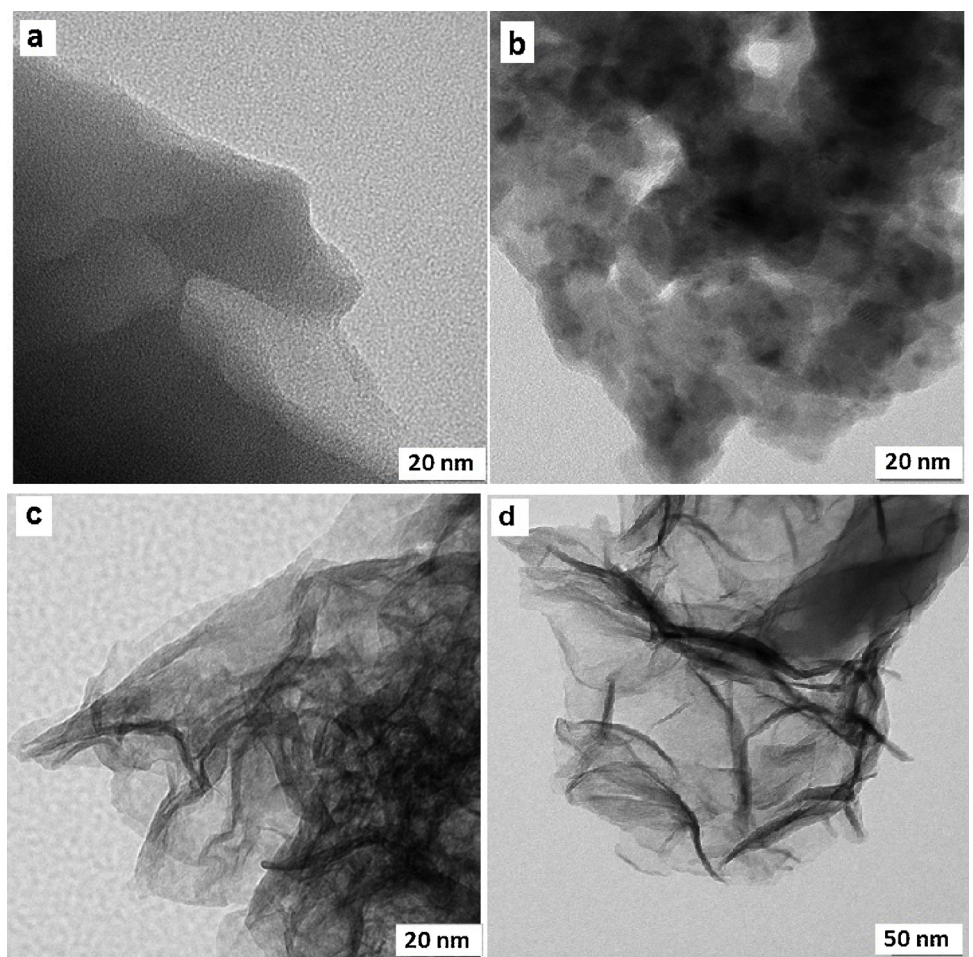


Fig. 3. TEM images of pristine g-C<sub>3</sub>N<sub>4</sub> (a) and the Cu/CN (b), Ni/CN (c), and Cu-Ni/CN (d) nanocomposites.

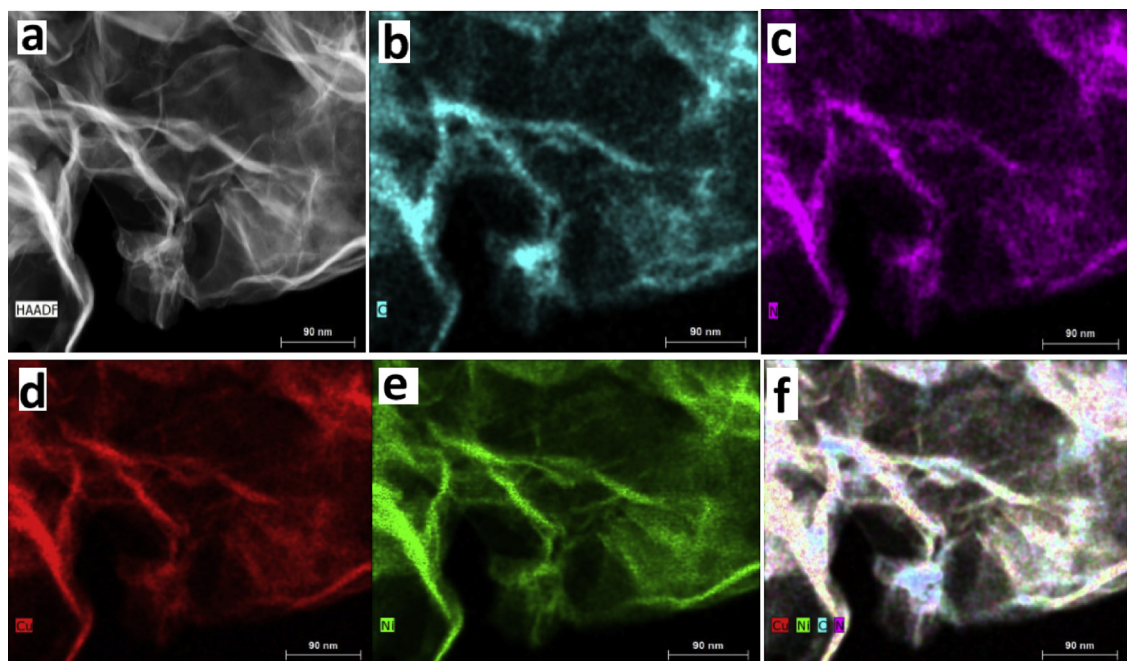


Fig. 4. HAADF image (a) and elemental mappings (b–f) of C, N, Cu, Ni and Cu/Ni/C/N in CuNi/g-C<sub>3</sub>N<sub>4</sub> nanoparticles.

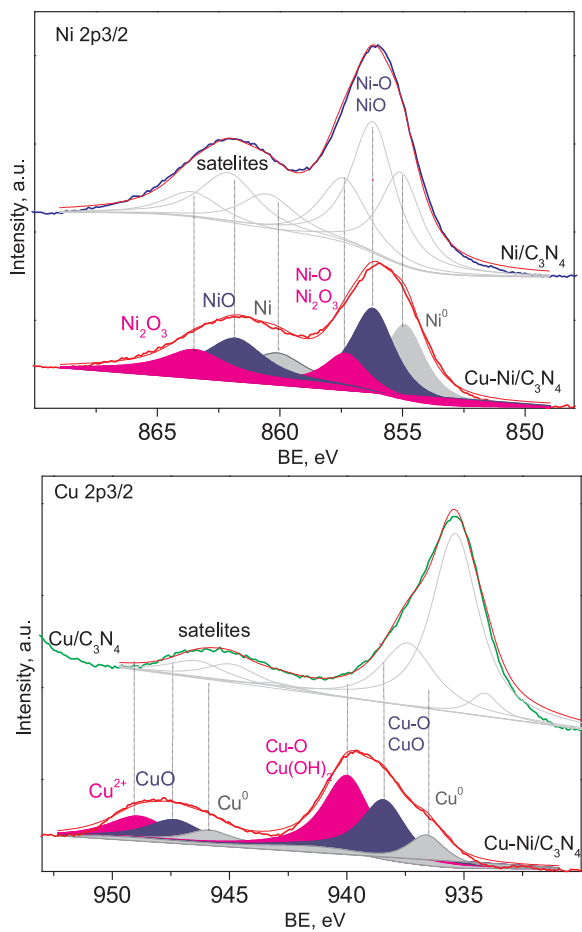


Fig. 5. XPS spectra survey and core levels for Ni2p and Cu2p.

data agree well with the microscopic and XRD data, which indicated the presence of finely dispersed Ni particles, mostly in the form of NiO and  $\text{Ni}_2\text{O}_3$ . The greater peak intensity increase in O 1s region for the Cu- and Ni-modified samples was thus due to the formation of these oxides and a greater content of adsorbed water compared to the parent CN sample [52].

The ATR spectra of all four samples are represented in Fig. S3a. For all studied samples, five main regions can be identified in the frequency ranges between: (1) 3000–3200  $\text{cm}^{-1}$ , characteristic for  $-\text{N}-\text{H}$  stretching; (2) 2100–2700  $\text{cm}^{-1}$ , characteristic for conjugated and terminal bonds between carbon and nitrogen; (3) 1650–1540  $\text{cm}^{-1}$ , characteristic for  $\text{C}=\text{N}$  stretching vibrations; (4) 1400–1200  $\text{cm}^{-1}$ , characteristic for the aromatic  $\text{C}-\text{N}$  stretching and (5) 800–700  $\text{cm}^{-1}$ , characteristic for the vibration of CN heterocycles of triazine ring [57,58].

The most detailed analysis of ATR spectra of bare CN sample (Fig. S3a) are assigned as follows. The peak at 805  $\text{cm}^{-1}$  was attributed to the ring vibrational modes of s-triazine units [55,59,60]. The peaks between 1100–1750  $\text{cm}^{-1}$  (with maxima at 1726, 1596, 1507, 1348, 1283 and 1138  $\text{cm}^{-1}$ ) are characteristic of s-triazine vibrational modes such as  $\text{C}-\text{N}$  and  $\text{C}=\text{N}$  stretching, confirming the presence of chemical bonding between carbon and nitrogen in the CN structure [60,61]. The small peaks at 2155 and 2745  $\text{cm}^{-1}$  can be assigned to terminal cyano ( $\text{C}-\text{N}$ ) groups, conjugated double bonds ( $-\text{N}=\text{C}=\text{N}$ ), and similar species. [60,62] The broad set of peaks at higher wavenumbers (between 3000 and 3300  $\text{cm}^{-1}$ ) can be attributed to the stretching vibrational modes of primary ( $-\text{NH}_2$ ) and secondary ( $-\text{NH}_3$ ) amines as well as amine bridges, revealing that some nitrogen centers in the CN sample were hydrogenated as suggested previously [57,58,60,63].

The Cu and Ni-modified materials present the same absorption

bands observed for g- $\text{C}_3\text{N}_4$ , indicating that the triazine-based chemical structure is preserved. While comparing bare CN with Cu/CN, Ni/CN and Cu-Ni/CN catalysts we can observe that, CN modification by Cu and Ni influences the peak sharpness and intensity, but does not shift peaks maxima. In the region characteristic for s-triazine vibrational modes (1100–1750  $\text{cm}^{-1}$ ) the most pronounced change was observed for Cu-Ni/CN catalyst, while very small differences (if any) was detected between Ni/CN and bare CN sample. In contrary, both Ni and Cu modification influences the broad feature intensity in the region 3000–3200  $\text{cm}^{-1}$ . For Cu-Ni/CN the intensity was the highest one, while for Ni/CN the intensity was less compared to bare CN sample. This indicates that the CN modification by Cu NPs most likely influences the chemical bonding between carbon and nitrogen in the CN structure while Ni NPs most likely decrease the hydrogenation level of nitrogen centers in the CN sample. These findings correlate well with our XPS results (where the number OH species increased for Ni/CN) and previous study for carbon nitrides [58]. The previous data for polymeric  $\text{C}_x\text{N}_y\text{H}_z$  materials obtained via precursor thermolysis supported by comparison with reference compounds such as s-triazine ( $\text{C}_3\text{N}_3\text{H}_3$ ), melamine ( $\text{C}_3\text{N}_3(\text{NH}_2)_3$ ), melem ( $\text{C}_6\text{N}_7(\text{NH}_2)_3$ ) indicated similarities, especially taking into account the featured a broad set of intense peaks between 800 and 1750  $\text{cm}^{-1}$ . Moreover, it was shown that, the presence of sharp peaks at wavenumber values above 3000  $\text{cm}^{-1}$  may be indicative for well-ordered structures with limited N–H sites and H-bonding between neighboring units [58].

Raman spectroscopy was used to study the carbon materials' vibrational properties; the resulting spectra are presented in Fig. S3b. None of the studied nanocomposites exhibited clear characteristic peaks at ca. 1370 and 1570  $\text{cm}^{-1}$  that could be attributed to the D (for disordered) and G (for graphite) bands seen in the spectra of  $\text{sp}^2$  carbon materials [54,60]. The bands observed at 1616, 1555, 1481, 1234, 751, 705, 543, and 479  $\text{cm}^{-1}$  are characteristic of bulk g- $\text{C}_3\text{N}_4$ , corresponding to the vibration modes of CN heterocycles. The peak at 1234  $\text{cm}^{-1}$  in the Raman spectrum of CN was blue-shifted in the spectrum of the Ni/CN sample, suggesting that the C–N bonds in the nanocomposite were stronger than those in the parent material. A similar shift was reported for a modified framework of heptazine units in which some nitrogen centers were replaced with carbon; [56] in that case, the shift was attributed to the difference in electronegativity between carbon and nitrogen, which was suggested to strengthen the C–N bonds adjacent to the introduced carbon centers. Another study ascribed this band to  $=\text{C}(\text{sp}^2)$  bending vibrations [45], and attributed the blue shift to phonon confinement and strong quantum confinement effects in the exfoliated nanosheets, implying that they were ultrathin. However, it was difficult to precisely determine the number of layers in the samples from their Raman spectra. It has been reported that as the number of layers in the sample decreases, the intensity of the 479  $\text{cm}^{-1}$  peak also decreases but that of the 543  $\text{cm}^{-1}$  peak increases; accordingly, the  $I_{543}/I_{479}$  ratio increased rapidly from 0.1 for bulk coplanar g-h-heptazine- $\text{C}_3\text{N}_4$  to 1.2 for single-layered samples [45]. Similarly, the  $I_{751}/I_{705}$  ratio of bulk coplanar g-h-heptazine- $\text{C}_3\text{N}_4$  was only 0.4, but that for single-layered material was 1.0 [45]. The Cu- and/or Ni-modified nanocomposites likewise exhibited a blue shift of the 1234  $\text{cm}^{-1}$  peak (Ni/CN) and an increase in the intensity of the 543  $\text{cm}^{-1}$  peak, but the intensity of the 479  $\text{cm}^{-1}$  peak also increased, and the  $I_{745}/I_{705}$  ratios for these materials were in the range 0.2–0.5. This suggests the presence of bulk CN. Moreover, the modified nanocomposites (especially Cu-Ni/CN) exhibited a general increase in Raman intensity relative to the parent material, CN. Studies on Ag nanostructures have shown that the intensity of Raman spectra can be greatly enhanced by electromagnetic interactions or couplings between nanoparticles of certain shapes and sizes [54,60]. Graphite-like materials have the potential to exhibit similar Raman-enhancing effects. These Raman enhancements can be divided into three classes based on the symmetry of the molecule's vibrations [54]. In the case of the Ag nanoparticles, the Raman intensity enhancement was attributed to charge transfer

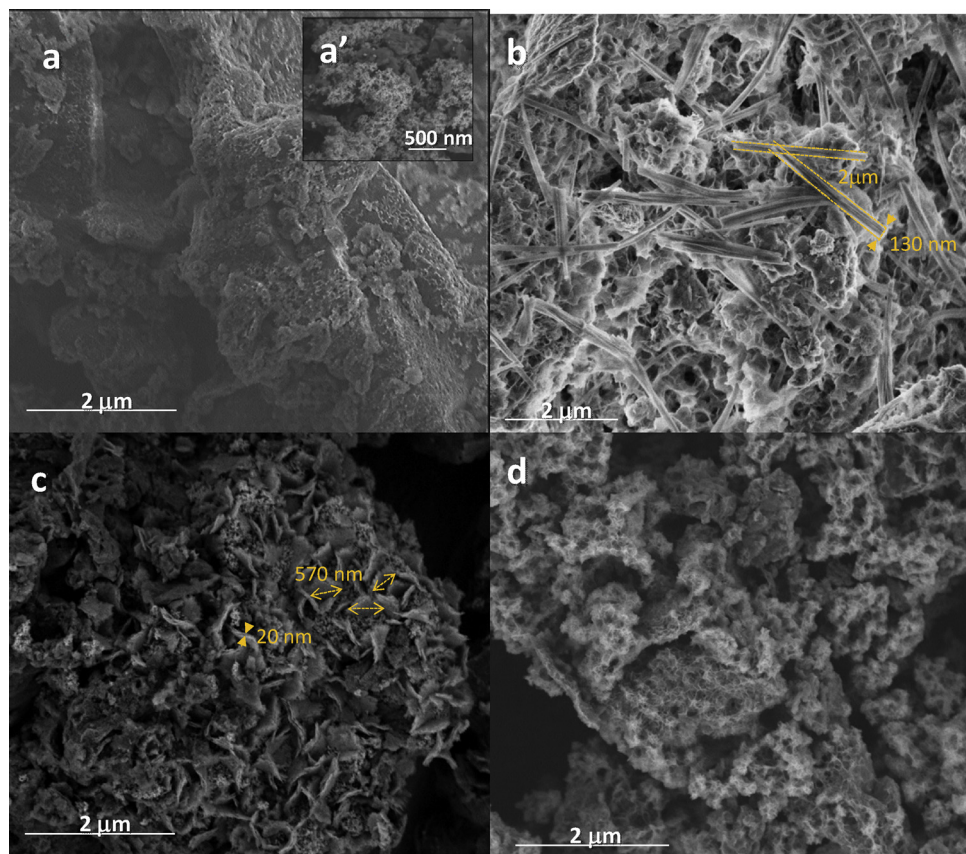


Fig. 6. (a–c) SEM images of GC electrodes with dropcasted catalysts layers.

between Ag and g-C<sub>3</sub>N<sub>4</sub>, originating from the plasma and Raman enhancement effects of Ag nanoparticles and g-C<sub>3</sub>N<sub>4</sub> molecules. The results presented here for Cu- and Ni-modified nanocomposites clearly demonstrate that g-C<sub>3</sub>N<sub>4</sub> molecules form similar charge transfer-facilitating interactions with Cu and Ni.

### 3.2. Morphology of nanostructured electrodes characterization

The morphology of the prepared GC electrodes by dropcasting technique was investigated by SEM, as shown in Fig. 6. A typical 2D sheet-like structure with wrinkles was clearly evident in the pristine CN (Fig. 2a, a') and was preserved when the transition metals were incorporated. It is worth noting that Ni, Cu or Cu-Ni incorporation resulted in transition metal segregation to the CN surface and nanostructure formation. Depending on the transition metal used, different nanostructures were observed over the CN support. For Cu-Ni/CN nanocomposite, typically the nanobelts with segregated microstructures composed by CuO (detected also by XRD) were formed with an average size of 2 μm and thickness of 130 nm. For Cu/CN nanocomposites, the nanoflakes were grown between the 2D sheet-like CN structure with an average size of 570 nm and thickness of 20 nm. The smallest change in CN morphology was observed for Ni/CN, where Ni nanoparticles were finely dispersed in 2D layered CN. The Ni particles size stayed below 2 nm, suggesting that the g-C<sub>3</sub>N<sub>4</sub> nanosheets may be good supports for preparing Ni nanoparticles.

### 3.3. Electrocatalytic methanol oxidation

The nanocomposites' effects on the electrocatalytic oxidation of methanol are shown in Fig. 7. Cyclic voltammetry (CV) and electrochemical impedance spectroscopy (EIS) were used to study the MOR at glassy carbon (GC) electrodes modified with Ni/CN, Cu-Ni/CN, Cu/CN,

and CN (results for the CN/GC system are presented in Fig. S5 of the Supporting information). Fig. 7(panels a–c) shows cyclic voltammograms recorded in 1.0 M NaOH containing different concentrations of methanol at a scan rate of 50 mVs<sup>-1</sup>. The polarization was initially increased from 0 to 0.80 V in the anodic direction, after which the scan was reversed in the cathodic direction and the polarization was returned to 0 V. The CV measurements were performed until no changes in the CV curves were observed. As shown in Fig. 7, no peak was observed for modified GC electrodes in the absence of methanol (shown by the black curves in panels a, b, and c). All electrodes exhibited increased current density as the methanol concentration increased, but strong anodic peaks associated with methanol electrooxidation were only observed for Ni-containing catalysts (Fig. 7a and b). This suggests that Ni nanoparticles are responsible for the electrocatalytic oxidation of methanol at the electrode surface. [34] This behavior is also reflected in the Nyquist plots of the impedance spectra recorded under the same conditions as the CV curves (panels a', b', and c' in Fig. 7). These spectra were collected at an applied potential of 0.5 V over a frequency range of 0.1 to 100 kHz with an AC signal amplitude of 5 mV. For all electrodes, the charge transfer resistance ( $R_{ct}$ ) for methanol electrooxidation decreased as the methanol concentration increased, causing the diameter of the semicircular part of the Nyquist plot to decrease as the methanol concentration increased. Fig. 8 compares CV and EIS measurements performed using different modified electrodes in the presence of 3.0 M methanol. Even though the total mass of transition metals in the Ni/CN catalyst is lower than that in the Cu-Ni/CN catalyst, the current density and  $R_{ct}$  observed with the former catalyst were around 6 times greater and 3 orders of magnitude lower, respectively, than those observed with the latter. Moreover, the onset of methanol electrooxidation was shifted to a less positive potential (~30 mV) when using the Ni/CN catalyst, suggesting that the Cu-free catalyst has greater electrocatalytic activity. The presence of the Cu nanoparticles clearly reduces the Ni-

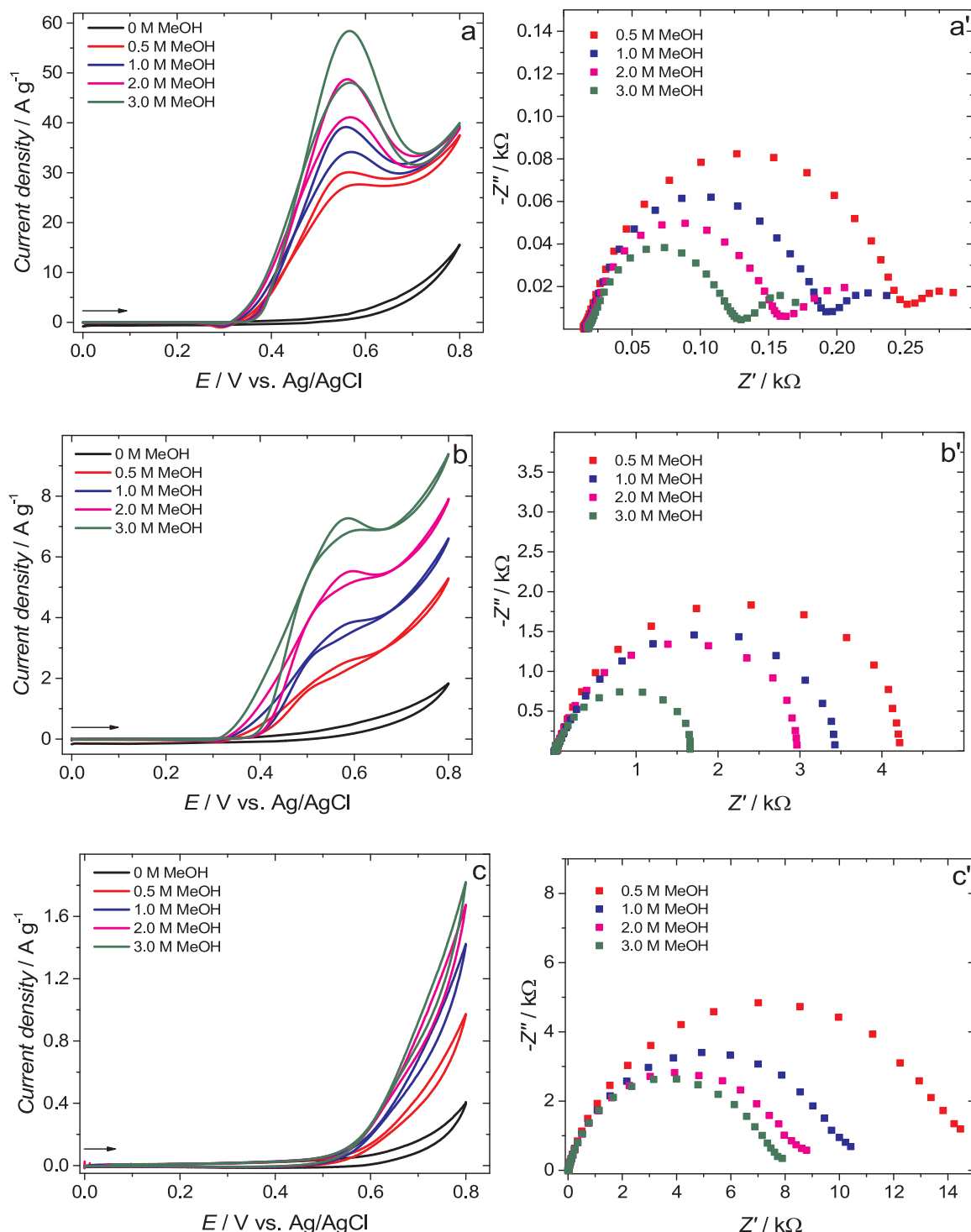


**Fig. 7.** CV curves (a–c) and Nyquist plots (a'–c') for GC electrodes modified with Ni/CN (a, a'), (Ni-Cu)/CN (b, b'), and Cu/CN (c, c') at various MeOH concentrations in 1 M NaOH. CV experiments were performed at the potential scan rate of  $50 \text{ mV s}^{-1}$ . Insets show the onset of methanol electrooxidation. EIS spectra were recorded at 0.5 V.

based catalyst's activity. This effect could be explained by several issues including observed differences in the nanocomposites' physicochemical properties and surface morphology what can influence the efficient adsorption of  $\text{OH}^-$  and  $\text{CH}_3\text{OH}$  by the surface groups. Also for Cu-modified electrodes a segregation of  $\text{CuO}$  is observed and agglomerated structures formation has been seen by SEM (Fig. 6) as well as by XRD measurement; sharp signals from monoclinic  $\text{CuO}$  JCPDS 41-0254 (Fig. 2). Moreover, Cu increases the charge transfer resistance and potential onset for MOR. For Ni/CN the anodic peak is observed at

564 mV whereas cathodic peak is observed at 557 mV. While Cu is incorporated in Ni-Cu/CN, the redox peak shifts to higher potential with an increase of 10 mV. For Ni-Cu/CN the anodic peak during forward and cathodic peak during backward scans are observed at 574 and 508 mV, respectively. This may suggest that the optimal Ni:Cu ratio was also not attained for mixed Ni-Cu/CN catalyst resulting increase of onset potential for MOR, charge transfer resistance and drop of current density. Previous study for Ni-Cu mesoporous zeolites (MesoZ) reported that while an optimum amount of  $\text{Ni}^{2+}$  and  $\text{Cu}^{2+}$  in MesoZ matrix was

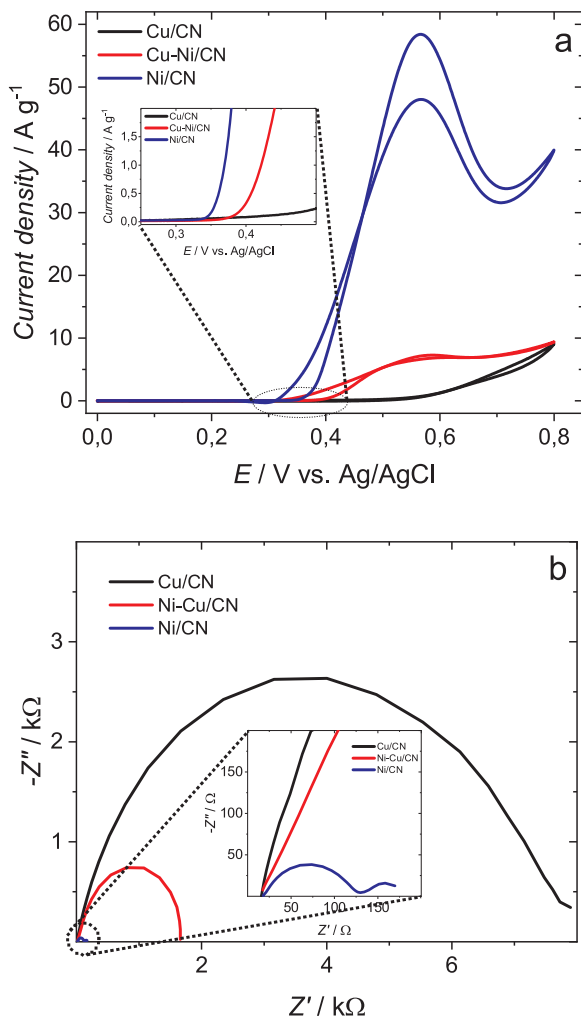


**Fig. 8.** CV curves (a) and Nyquist plots (b) for the GC electrode modified with Ni/CN (blue), Cu-Ni/CN (red), and Cu/CN (black) catalysts in 3.0 M methanol containing 1 M NaOH. CV curves were acquired at a potential scan rate of 50 mV s<sup>-1</sup>. EIS spectra were collected at 0.5 V. Insets show expansions of the CV curves showing the onset of methanol electrooxidation (a) and the Nyquist plot showing details of the EIS spectrum for the GC electrode modified with Ni/CN (For interpretation of the references to colour in this figure legend, the reader is referred to the web version of this article).

incorporated Cu<sup>2+</sup> facilitates the reduction of the onset potential whereas Ni<sup>2+</sup> effectively enhances the current density during methanol oxidation. It was found that, the that suitable amount of Ni<sup>2+</sup> and Cu<sup>2+</sup> notably influences the electron transfer rate and accelerates the diffusion of ferri/ferrocyanide redox couple towards the electrode interface [64]. Similarly for CoCu alloy nanoparticles-incorporated carbon nanofibers obtained by electrospinning an optimum composition Cu5%Co95% was found [65]. According to the obtained results, the observed electrocatalytic activity of Cu5%Co95% was attributed to formation of ZOOH/Z(OH)<sub>2</sub> on the surface of the Z alloy (Z refers to the optimum composition (Cu5%Co95%)) [65].

The stability of GC electrodes modified with the different nanocomposites was examined under chronoamperometric conditions by recording the current at a fixed potential ( $E = 0.5$  V) in 3.0 M methanol containing 1.0 M NaOH (Fig. 9). With the Ni/CN electrode, the current density fell slightly (by ~7%) after ~20 min and then remained steady. This indicates that the Ni/CN catalyst exhibits stable electrocatalytic activity. The Cu-Ni/CN and Cu/CN electrodes were less stable: the current density decreased by about 18 and 40% respectively, after 40 min under the applied potential, after which no further changes

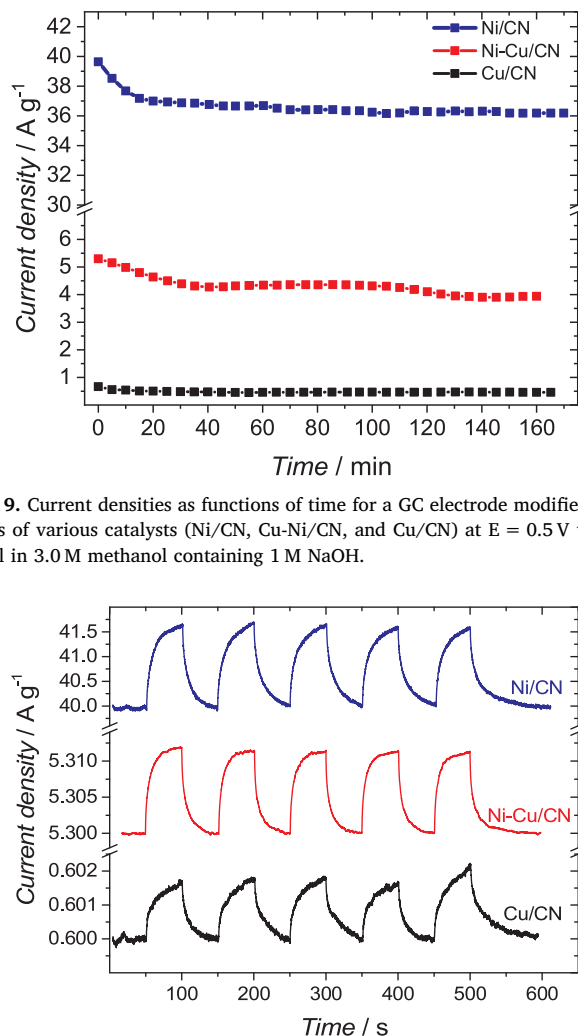


**Fig. 9.** Current densities as functions of time for a GC electrode modified with films of various catalysts (Ni/CN, Cu-Ni/CN, and Cu/CN) at  $E = 0.5$  V vs Ag/AgCl in 3.0 M methanol containing 1 M NaOH.

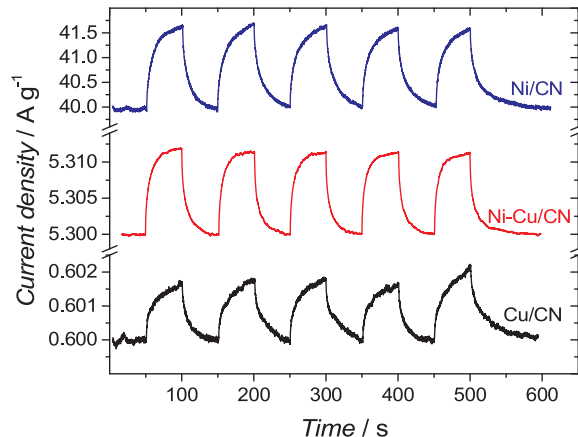


**Fig. 10.** Current densities achieved with Ni/CN-, Cu-Ni/CN-, and Cu/CN-modified electrodes in darkness and under visible light illumination.

were observed.

Finally, the catalysts' photocatalytic activity was investigated in a 3.0 M solution of methanol containing 1 M NaOH under CV and EIS conditions Figs. 10 and S7. Fig. 10 shows photocurrent-time curves recorded at a fixed potential of 0.5 V vs. Ag/AgCl during on/off cycles upon visible light illumination. All electrodes exhibited a responsive photocurrent upon visible light illumination. As expected, the Ni/CN electrode's current density was much higher than that for the Cu-Ni/CN and Cu/CN systems. Upon illumination, the current densities for the Ni/CN, Cu-Ni/CN, and Cu/CN electrodes increased by ~1.8, ~0.01, and ~0.001 A g<sup>-1</sup>, respectively, revealing that the photoelectroactivity of the Ni/CN catalyst is over 100 times greater than that of the Cu-containing catalysts. The very weak increase in current densities for the Cu-containing system was attributed to poor stability of CuO as photocatalysts and regarding Cu<sub>2</sub>O phase a fast Cu<sup>+</sup> reduction/oxidation to Cu<sup>0</sup> and Cu<sup>2+</sup> [2,38]. A control experiment with a CN/GC electrode yielded a responsive photocurrent increase of ~0.05 A g<sup>-1</sup> (Fig. S3, Supporting information). Notably, the catalytic performance of the Ni/CN nanocomposite in the MOR is better than or comparable to that of previously reported noble and non-noble metal catalysts (Table S2).

An earlier publication on NiO electrodeposited on multiwalled carbon nanotubes (NiO/MWCNT) explained the electrochemical MOR over Ni(II) and Ni(III) species using the following mechanism [34,35]:



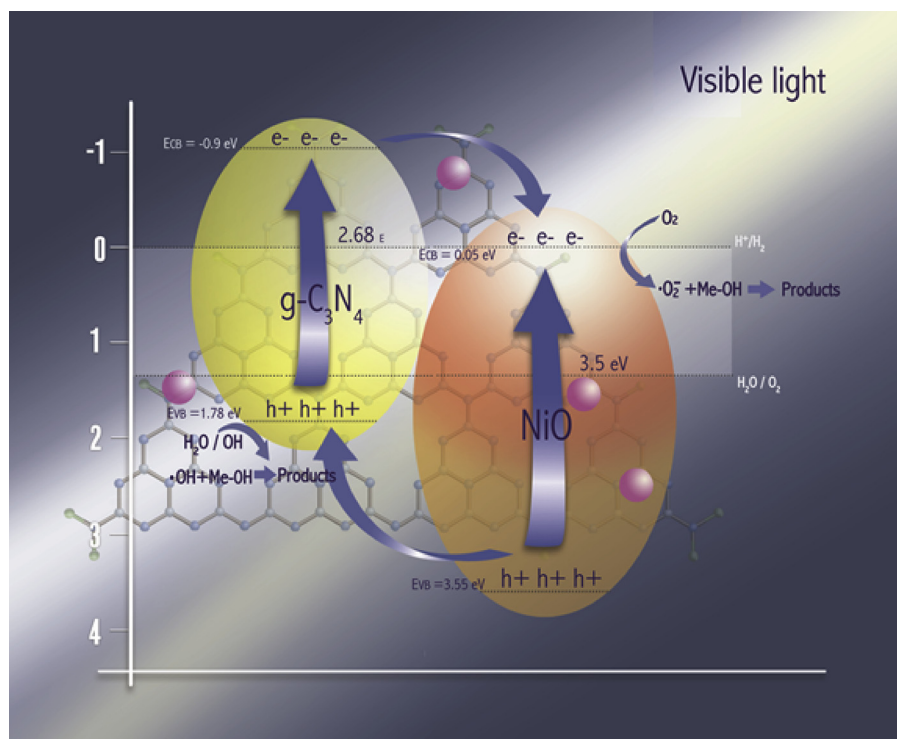


Fig. 11. A schematic illustration of methanol photoelectrooxidation on the Ni/CN composite under visible light illumination.



Reaction (1) corresponds to the potential region around  $\sim 0.4$  V, at which Ni(III) species are generated. At this potential, it was proposed that methanol oxidation appears as a moderate increase in current density. These results clearly show that Ni participates directly in this electrocatalytic methanol oxidation process. In the region around  $\sim 0.6$  V, at which only Ni(III) species exist at the electrode surface, a new anodic peak was usually observed with a larger peak current than that seen at the lower potential (Reaction (6)) [34,35]. The height of this peak increases linearly with the methanol concentration in the solution, showing that it is related to a process involving methanol, in good agreement with previous reports [34,35]. It was concluded that methanol oxidation primarily occurs after the complete oxidation of Ni (II) to Ni(III), and proceeds via the interconversion of Ni(II) and Ni(III) at the switching potential [34].

This strongly supports the previously suggested catalytic role of Ni (III) in methanol oxidation. The effects of the nanocomposites' surface morphology, and the type and size of the Cu- and/or Ni-modified nanostructures, correlate well with their observed MOR efficiencies. As was predicted, finely dispersed Ni nanoparticles were most efficient. The electrochemical data correlate well with the XPS observations (the BE shift in C1s for modified CN and amount of  $-\text{OH}$  groups detected for Ni/CN was the highest one), which suggest that the changes in electronic structure induced by the presence of Ni nanostructures reduce the energetic barriers to methanol adsorption on the Ni/CN surface, resulting in high MOR catalytic activity. The use of ultrathin CN as a support prevented Ni aggregation during nanocomposite synthesis, yielding a product containing small Ni nanoparticles that are stabilized during catalysis. Moreover, the 2D nanosheet-like structure of the resulting material should favor the adsorption of reacting molecules [14]. The layered nanostructured form of the hybrid materials together with their stable dispersions of metal centers provide catalytically active sites, facilitating the access of reactants (relevant species) and the quick release of product(s) (gas bubbles) from the catalyst surface [66]. It has

been shown that visible light irradiation can increase the performance of modified and bare CN electrodes in the MOR via synergistic electro- and photo-catalytic oxidation [14,67], and such an effect was observed in the present work for Ni/CN ( $127 \text{ A g}^{-1}$ )  $>$  Cu-Ni/CN ( $7.14 \text{ A g}^{-1}$ )  $>$  Cu/CN ( $1.71 \text{ A g}^{-1}$ ) catalysts. This synergy is also well seen when comparing charge transfer resistance during MOR for modified electrodes under dark and visible light illumination (Fig. S7). In all cases a decrease in  $Z'$  is observed (most pronounced decrease in  $Z'$  for Ni/CN ca. 50%) suggesting facilitation MOR reaction. The reaction mechanism can be proposed in Fig. 11, similarly as for Pt/g-C<sub>3</sub>N<sub>4</sub> electrode [14,68]. When modified CN catalyst was irradiated with visible light ( $> 400 \text{ nm}$ ), the g-C<sub>3</sub>N<sub>4</sub> was excited, causing the spontaneous generation of electrons ( $e_{\text{CB}}^-$ ) in the conduction band (CB) and holes ( $h_{\text{VB}}^+$ ) in the valence band (VB). The holes were reported to be oxidizing and to react with surface-adsorbed OH-/H<sub>2</sub>O to form strongly oxidizing hydroxyl radicals ('OHs) that could in turn react with methanol molecules adsorbed on the catalyst surface, resulting in a photocatalytic MOR process. Electron-hole pairs usually recombine quickly, so only a fraction of the holes formed in this way will be available for photo-electrocatalysis [14,69]. The photocurrent responses observed for Cu- and/or Ni-modified nanocomposites (Figs. 10 and S7) demonstrated that interfacial charge transfer occurs between photoexcited g-C<sub>3</sub>N<sub>4</sub> nanosheets and Cu- and/or Ni-modified nanostructures, similar to that seen with Pt-modified electrodes [14, 70–73]. These excited electrons are probably initially transferred to the transition metal centers and then flow to the circuit under the influence of the external electric field, preventing charge recombination.

#### 4. Conclusions

Different Ni, Cu and Cu-Ni nanostructures have been fabricated and homogeneously embedded on ultrathin two-dimensional (2D) carbon nitride (g-C<sub>3</sub>N<sub>4</sub>). The above results demonstrate that finely tuned noble-metal-free nanostructures, and especially the Ni/CN system reported here, can be used as electrocatalysts with high MOR efficiency, stability, and performance for the electrooxidation of methanol in DMFC application. The current densities obtained for 4% (wt.%) Ni/CN, Cu-

Ni/CN and Cu/CN electrocatalysts were 5879, 551 and  $1.71 \text{ A g}^{-1}$  rivalling stable MOR activity under alkaline conditions (Table S2). Moreover, there is considerable scope for tuning their performance and properties by adjusting the stoichiometry of the transition metals as well as the chemical composition and morphology of the nanocomposite surface to regulate the current density and photocurrent. Given the ease of fabrication and low cost of both the nanocomposites and the electrodes used in these systems, the results presented herein reveal a promising class of highly efficient photo-electrocatalysts for the oxidation of small organic molecules.

## Acknowledgment

The present research was financially supported by the Foundation for Polish Science co-financed by the European Regional Development Fund under the Smart Growth Operational Programme PO IR (project no. REINTEGRATION/2016-1/5). MG and RZ gratefully acknowledge financial support from the Ministry of Education, Youth and Sports of the Czech Republic under the Operational Program Research, Development and Education - European Regional Development Fund (project no. CZ.02.1.01/0.0/0.0/16\_019/0000754) and the assistance provided by the Research Infrastructures NanoEnviCz under project LM2015073. The authors thank Ondrej Tomanec for HRTEM-elemental mapping data.

## Appendix A. Supplementary data

Supplementary material related to this article can be found, in the online version, at doi:<https://doi.org/10.1016/j.apcatb.2018.10.072>.

## References

- J.C. Colmenares, R.F. Colmenares Quintero, I.S. Pieta, Catalytic dry reforming for biomass-based fuels processing: progress and future perspectives, *Energy Technol.* 4 (2016) 881–890.
- M.B. Gawande, A. Goswami, F.X. Felpin, T. Asefa, X. Huang, R. Silva, X. Zou, R. Zboril, R.S. Varma, Cu and Cu-based nanoparticles: synthesis and applications in catalysis, *Chem. Rev.* 116 (2016) 3722–3811.
- A. Goswami, A.K. Rathi, C. Aparicio, O. Tomanec, M. Petr, R. Pocklanova, M.B. Gawande, R.S. Varma, R. Zboril, In situ generation of Pd–Pt core–shell nanoparticles on reduced graphene oxide (Pd@Pt/rGO) using microwaves: applications in dehalogenation reactions and reduction of olefins, *ACS Appl. Mater. Interfaces* 9 (2017) 2815–2824.
- X.-X. Lin, A.-J. Wang, K.-M. Fang, J. Yuan, J.-J. Feng, One-pot seedless aqueous synthesis of reduced graphene oxide (rGO)-supported core–shell Pt@Pd nano-flowers as advanced catalysts for oxygen reduction and hydrogen evolution, *ACS Sustain. Chem. Eng.* 5 (2017) 8675–8683.
- S. Zinoviev, F. Müller-Langer, P. Das, N. Bertero, P. Fornasiero, M. Kaltschmitt, G. Centi, S. Miertus, Next-generation biofuels: survey of emerging technologies and sustainability issues, *ChemSusChem* 3 (2010) 1106–1133.
- C. Agrafiotis, M. Roeb, C. Sattler, A review on solar thermal syngas production via redox pair-based water/carbon dioxide splitting thermochemical cycles, *Renew. Sustain. Energy Rev.* 42 (2015) 254–285.
- J. Rostrup-Nielsen, Syngas in perspective, *Catal. Today* 71 (2002) 243–247.
- G.C. Chinchen, P.J. Denny, D.G. Parker, M.S. Spencer, D.A. Whan, Mechanism of methanol synthesis from  $\text{CO}_2/\text{CO}/\text{H}_2$  mixtures over copper/zinc oxide/alumina catalysts: use of  $^{14}\text{C}$ -labelled reactants, *Appl. Catal.* 30 (1987) 333–338.
- B. Kaur, R. Srivastava, B. Satpati, Highly efficient  $\text{CeO}_2$  decorated nano-ZSM-5 catalyst for electrochemical oxidation of methanol, *ACS Catal.* 6 (4) (2016) 2654–2663.
- K. Waugh, Methanol synthesis, *Catal. Today* 15 (1992) 51–75.
- X. Zhen, Methanol as an internal combustion on engine fuel, in: A. Basile, F. Dalena (Eds.), *Methanol: Science and Engineering*, Elsevier B.V., 2017, pp. 313–337.
- Z.K. Ghouri, N.A.M. Barakat, H.Y. Kim, Synthesis and electrochemical properties of  $\text{MnO}_2$  and Co-decorated graphene as novel nanocomposite for electrochemical super capacitors application, *Energy Environ. Focus* 4 (2015) 34–39.
- C. Lu, P. Zhang, S. Jong, X. Wu, S. Song, M. Zhu, Z. Lou, Z. Li, F. Liu, Y. Lin, Y. Wang, Z. Le, Photocatalytic reduction elimination of  $\text{UO}_2^{2+}$  pollutant under visible light with metal-free sulfur doped g-C<sub>3</sub>N<sub>4</sub> photocatalyst, *Appl. Catal. B: Environ.* 200 (2017) 378–385.
- M. Zhu, C. Zhai, M. Sun, Y. Hu, B. Yan, Ultrathin graphitic C<sub>3</sub>N<sub>4</sub> nanosheet as a promising visible-light-activated support for boosting photoelectrocatalytic methanol oxidation, *Appl. Catal. B: Environ.* 203 (2017) 108–115.
- Z.K. Ghouri, N.A.M. Barakat, H.Y. Kim, Influence of copper content on the electrocatalytic activity toward methanol oxidation of Co chi Cuy alloy nanoparticles-decorated CNFs, *Sci. Rep.* 5 (2015).
- L. Lin, W. Zhou, R. Gao, S. Yao, X. Zhang, W. Xu, S. Zheng, Z. Jiang, Q. Yu, Y.-W. Li, C. Shi, X.-D. Wen, D. Ma, Low-temperature hydrogen production from water and methanol using Pt/α-MoC catalysts, *Nature* 544 (2017) 80–83.
- D.Y. Chung, K.J. Lee, Y.E. Sung, Methanol electro-oxidation on the Pt surface: revisiting the cyclic voltammetry interpretation, *J. Phys. Chem. C* 120 (2016) 9028–9035.
- Z.K. Ghouri, N.A.M. Barakat, M. Obaid, J.H. Lee, H.Y. Kim, Co/CeO<sub>2</sub>-decorated carbon nanofibers as effective non-precious electro-catalyst for fuel cells application in alkaline medium, *Ceram. Int.* 41 (2015) 2271–2278.
- G. Long, X. Li, K. Wan, Z. Liang, J. Piao, P. Tsikarous, Pt/CN-doped electrocatalysts: superior electrocatalytic activity for methanol oxidation reaction and mechanistic insight into interfacial enhancement, *Appl. Catal. B: Environ.* 203 (2017) 541–548.
- N.A.M. Barakat, M. Motlak, B.S. Kim, A.G. El-Deen, S.S. Al-Deyab, A.M. Hamza, Carbon nanofibers doped by  $\text{Ni}_{x}\text{Co}_{1-x}$  alloy nanoparticles as effective and stable non-precious electrocatalyst for methanol oxidation in alkaline media, *J. Mol. Catal. A: Chem.* 394 (2014) 177–187.
- A.G. El-Deen, N.A.M. Barakat, K.A. Khalil, M. Motlak, H.Y. Kim, Graphene/SnO<sub>2</sub> nanocomposite as an effective electrode material for saline water desalination using capacitive deionization, *Ceram. Int.* 40 (2014) 14627–14634.
- K. Klak, D. Marks, A. Wadas, M. Piatek, W. Lotowska, S. Zoladek, I.A. Rutkowska, P.J. Kulesza, Nanostructured hybrid electrocatalytic materials for ethanol oxidation: activation of Pt–Ru centers through modification with selected metal oxides, *ECS Trans.* 45 (2013) 13–24.
- P.J. Kulesza, I.S. Pieta, I.A. Rutkowska, A. Wadas, D. Marks, K. Klak, L. Stobinski, J.A. Cox, Electrocatalytic oxidation of small organic molecules in acid medium: enhancement of activity of noble metal nanoparticles and their alloys by supporting or modifying them with metal oxides, *Electrochim. Acta* 110 (2013) 474–483.
- N.A.M. Barakat, M.H. El-Newehy, A.S. Yasin, Z.K. Ghouri, S.S. Al-Deyab, Ni/Mn nanoparticles-decorated carbon nanofibers as effective electrocatalyst for urea oxidation, *Appl. Catal. A: Gen.* 510 (2016) 180–188.
- N.A.M. Barakat, M. Motlak, B.H. Lim, M.H. El-Newehy, S.S. Al-Deyab, Effective and stable CoNi alloy-loaded graphene for ethanol oxidation in alkaline medium, *J. Electrochem. Soc.* 161 (2014) F1194–F1201.
- H. Xu, P. Song, J. Wang, F. Gao, Y. Zhang, J. Guo, Y. Du, J. Di, Visible-light-improved catalytic performance for methanol oxidation based on plasmonic PtAu dendrites, *ChemElectroChem* 5 (2018) 1191–1196.
- H. Xu, B. Yan, K. Zhang, C. Wang, J. Zhong, S. Li, P. Yang, Y. Du, Facile synthesis of Pd–Ru–P ternary nanoparticle networks with enhanced electrocatalytic performance for methanol oxidation, *Int. J. Hydrogen Energy* 42 (2017) 11229–11238.
- L.M. Azofra, D.R. MacFarlane, C.H. Sun, A DFT study of planar vs. corrugated graphene-like carbon nitride (g-C<sub>3</sub>N<sub>4</sub>) and its role in the catalytic performance of CO<sub>2</sub> conversion, *Phys. Chem. Chem. Phys.* 18 (2016) 18507–18514.
- N.A.M. Barakat, M. Motlak, CoxNiy-decorated graphene as novel, stable and super effective non-precious electro-catalyst for methanol oxidation, *Appl. Catal. B: Environ.* 154 (2014) 221–231.
- Z.K. Ghouri, N.A.M. Barakat, A. Alam, M.S. Aloufi, T.M. Bawazeer, A.F. Mohamed, H.Y. Kim, Synthesis and characterization of nitrogen-doped & CaCO<sub>3</sub>-decorated reduced graphene oxide nanocomposite for electrochemical supercapacitors, *Electrochim. Acta* 184 (2015) 193–202.
- M. Garcia-Dieguez, I.S. Pieta, M.C. Herrera, M.A. Larrubia, L.J. Alemany, Nanostructured Pt- and Ni-based catalysts for CO<sub>2</sub>-reforming of methane, *J. Catal.* 270 (2010) 136–145.
- I.S. Pieta, W.S. Epling, M. Garcia-Dieguez, J.Y. Luo, M.A. Larrubia, M.C. Herrera, L.J. Alemany, Nanofibrous Pt–Ba Lean NO<sub>x</sub> trap catalyst with improved sulfur resistance and thermal durability, *Catal. Today* 175 (2011) 55–64.
- I.S. Pieta, M. Garcia-Dieguez, M.A. Larrubia, L.J. Alemany, W.S. Epling, Nanofiber alumina supported lean NO<sub>x</sub> trap: improved sulfur tolerance and NO<sub>x</sub> reduction, *Top. Catal.* 56 (2013) 50–55.
- M. Asgari, M.G. Maragheh, R. Davarkhah, E. Lohrasbi, Methanol electrooxidation on the nickel oxide nanoparticles/multi-walled carbon nanotubes modified glassy carbon electrode prepared using pulsed electrodeposition, *J. Electrochem. Soc.* 158 (2011) K225–K229.
- A. Seghiour, J. Chevalet, A. Barhoum, F. Lantelme, Electrochemical oxidation of nickel in alkaline solutions: a voltammetric study and modelling, *J. Electroanal. Chem.* 442 (1998) 113–123.
- Z. Wang, G. Zou, C. Feng, Y. Ma, X. Wang, Y. Bi, Novel composites of graphitic carbon nitride and NiO nanosheet arrays as effective photocathodes with enhanced photocurrent performances, *RSC Adv.* 86 (2016) 83350–83355.
- L. Liu, Y. Qi, J. Hu, Y. Liang, W. Cui, Efficient visible-light photocatalytic hydrogen evolution and enhanced photostability of core@shell Cu<sub>2</sub>O@g-C<sub>3</sub>N<sub>4</sub> octahedra, *Appl. Surf. Sci.* 351 (2015) 1146–1154.
- J. Chen, S. Shen, P. Guo, M. Wang, P. Wu, X. Wang, L. Guo, In-situ reduction synthesis of nano-sized Cu<sub>2</sub>O particles modifying g-C<sub>3</sub>N<sub>4</sub> for enhanced photocatalytic hydrogen production, *Appl. Catal. B: Environ.* 152–153 (2014) 335–341.
- D. Astruc, F. Lu, J.R. Aranzaes, Nanoparticles as recyclable catalysts: the frontier between homogeneous and heterogeneous catalysis, *Angew. Chem. Int. Ed.* 44 (2005) 7852–7872.
- C. Burda, X. Chen, R. Narayanan, M.A. El-Sayed, Chemistry and properties of nanocrystals of different shapes, *Chem. Rev.* 105 (2005) 1025–1102.
- S. Cao, Y. Yuan, J. Barber, S. Loo, C. Xue, Noble-metal-free g-C<sub>3</sub>N<sub>4</sub>/Ni(dmgH)<sub>2</sub> composite for efficient photocatalytic hydrogen evolution under visible light irradiation, *Appl. Surf. Sci.* 319 (2014) 344–349.
- X. Li, J. Zhu, B. Wei, Hybrid nanostructures of metal/two-dimensional nanomaterials for plasmon-enhanced applications, *Chem. Soc. Rev.* 45 (2016) 3145–3187.
- R. Jiang, B. Li, C. Fang, J. Wang, Metal/semiconductor hybrid nanostructures for plasmon-enhanced applications, *Adv. Mater.* 26 (2014) 5274–5309.

[44] Y. Fu, J. Zhu, C. Hu, X. Wu, X. Wang, Covalently coupled hybrid of graphitic carbon nitride with reduced graphene oxide as a superior performance lithium-ion battery anode, *Nanoscale* 6 (2014) 12555–12564.

[45] J. Jiang, L. Ou-yang, L. Zhu, A. Zheng, J. Zou, X. Yi, H. Tang, Dependence of electronic structure of g-C<sub>3</sub>N<sub>4</sub> on the layer number of its nanosheets: a study by Raman spectroscopy coupled with first-principles calculations, *Carbon* 80 (2014) 213–221.

[46] F. Su, S.C. Mathew, G. Lipner, X. Fu, M. Antonietti, S. Blechert, X. Wang, Mg<sub>2</sub>C<sub>3</sub>N<sub>4</sub>-catalyzed selective oxidation of alcohols using O<sub>2</sub> and visible light, *J. Am. Chem. Soc.* 132 (2010) 16299–16301.

[47] Y. Wang, X. Wang, M. Antonietti, Polymeric graphitic carbon nitride as a heterogeneous organocatalyst: from photochemistry to multipurpose catalysis to sustainable chemistry, *Angew. Chem. Int. Ed.* 51 (2012) 68–89.

[48] S. Zhang, S. Tsuzuki, K. Ueno, K. Dokko, M. Watanabe, Upper limit of nitrogen content in carbon materials, *Angew. Chem. Int. Ed.* 54 (2015) 1302–1306.

[49] M. Abdollahifar, M. Haghghi, A.A. Babaloo, Syngas production via dry reforming of methane over Ni/Al<sub>2</sub>O<sub>3</sub>–MgO nanocatalyst synthesized using ultrasound energy, *J. Ind. Eng. Chem.* 20 (2014) 1845–1851.

[50] P. Rzeszotarski, Z. Kaszkur, Surface reconstruction of Pt nanocrystals interacting with gas atmosphere. Bridging the pressure gap with in situ diffraction, *Phys. Chem. Chem. Phys.* 11 (2009) 5416–5421.

[51] Q. Liu, C. Fan, H. Tang, X. Sun, J. Yang, X. Cheng, One-pot synthesis of g-C<sub>3</sub>N<sub>4</sub>/V<sub>2</sub>O<sub>5</sub> composites for visible light-driven photocatalytic activity, *Appl. Surf. Sci.* 358 (2015) 188–195.

[52] H. Xu, J. Yan, X. She, L. Xu, J. Xia, Y. Xu, Y. Song, L. Huang, H. Li, Graphene-analogue carbon nitride: novel exfoliation synthesis and its application in photocatalysis and photoelectrochemical selective detection of trace amount of Cu<sup>2+</sup>, *Nanoscale* 6 (2014) 1406–1415.

[53] F. Dong, Z. Zhao, T. Xiong, Z. Ni, W. Zhang, Y. Sun, W. Ho, In situ construction of g-C<sub>3</sub>N<sub>4</sub>/g-C<sub>3</sub>N<sub>4</sub> metal-free heterojunction for enhanced visible-light photocatalysis, *ACS Appl. Mater. Interfaces* 5 (2013) 11392–11401.

[54] H. Li, Y. Jing, X. Ma, T. Liu, L. Yang, B. Liu, S. Yin, Y. Wei, Y. Wang, Construction of a well-dispersed Ag/graphene-like g-C<sub>3</sub>N<sub>4</sub> photocatalyst and enhanced visible light photocatalytic activity, *RSC Adv.* 7 (2017) 8688–8693.

[55] W. Zhang, H. Huang, F. Li, K. Deng, X. Wang, Palladium nanoparticles supported on graphitic carbon nitride-modified reduced graphene oxide as highly efficient catalysts for formic acid and methanol electrooxidation, *J. Mater. Chem. A* 2 (2014) 19084–19094.

[56] W. Ho, Z. Zhang, W. Lin, S. Huang, X. Zhang, X. Wang, Y. Huang, Copolymerization with 2,4,6-triaminopyrimidine for the rolling-up the layer structure, tunable electronic properties, and photocatalysis of g-C<sub>3</sub>N<sub>4</sub>, *ACS Appl. Mater. Interfaces* 7 (2015) 5497–5505.

[57] M.J. Lima, A.M.T. Silva, C.G. Silva, J.L. Faria, Graphitic carbon nitride modified by thermal, chemical and mechanical processes as metal-free photocatalyst for the selective synthesis of benzaldehyde from benzyl alcohol, *J. Catal.* 353 (2017) 44–53.

[58] T.S. Miller, A.B. Jorge, T.M. Suter, A. Sella, F. Cora, P.F. McMillan, Carbon nitrides: synthesis and characterization of a new class of functional materials, *Phys. Chem. Chem. Phys.* 19 (2017) 15613–15638.

[59] Q.X. Guo, Y. Xie, X.J. Wang, S.C. Lv, T. Hou, X.M. Liu, Characterization of well-crystallized graphitic carbon nitride nanocrystallites via a benzene-thermal route at low temperatures, *Chem. Phys. Lett.* 380 (2003) 84–87.

[60] F. Yang, V. Kuznetsov, M. Lublow, C. Merschjann, A. Steigert, J. Klaer, A. Thomas, T. Schedel-Niedrig, Solar hydrogen evolution using metal-free photocatalytic polymeric carbon nitride/CuInS<sub>2</sub> composites as photocathodes, *J. Mater. Chem. A* 1 (2013) 6407–6415.

[61] S.M. Lyth, Y. Nabae, S. Moriya, S. Kuroki, M. Kakimoto, J. Ozaki, S. Miyata, Carbon nitride as a nonprecious catalyst for electrochemical oxygen reduction, *J. Phys. Chem. C* 113 (2009) 20148–22015.

[62] E.G. Gillan, Synthesis of nitrogen-rich carbon nitride networks from an energetic molecular azide precursor, *Chem. Mater.* 12 (2000) 3906–3912.

[63] J.L. Zimmerman, R. Williams, V.N. Khabashesku, J.L. Margrave, Synthesis of spherical carbon nitride nanostructures, *Nano Lett.* 1 (2001) 731–734.

[64] Z.K. Ghouri, N.A.M. Barakat, H.Y. Kim, Influence of copper content on the electrocatalytic activity toward methanol oxidation of Co<sub>x</sub>Cu<sub>y</sub> alloy nanoparticles-decorated CNFs, *Sci. Rep.* 5 (2015) 16695.

[65] S. Samanta, K. Bhunia, D. Pradhan, B. Satpathi, R. Srivastava, Ni and Cu ion-exchanged nanostructured mesoporous zeolite: a noble metal free, efficient, and durable electrocatalyst for alkaline methanol oxidation reaction, *Mater. Today Energy* 8 (2018) 45–56.

[66] B. Liu, Y.F. Zhao, H.Q. Peng, Z.Y. Zhang, C.K. Sit, M.F. Yuen, T.R. Zhang, C.S. Lee, W.J. Zhang, Nickel–cobalt diselenide 3D mesoporous nanosheet networks supported on Ni foam: an all-pH highly efficient integrated electrocatalyst for hydrogen evolution, *Adv. Mater.* 29 (2017) 1606521.

[67] K. Drew, G. Girishkumar, K. Vinodgopal, P.V. Kamat, Boosting fuel cell performance with a semiconductor photocatalyst: TiO<sub>2</sub>/Pt–Ru hybrid catalyst for methanol oxidation, *J. Phys. Chem. B* 109 (2005) 11851–11857.

[68] X.H. Li, M. Antonietti, Metal nanoparticles at mesoporous N-doped carbons and carbon nitrides: functional Mott–Schottky heterojunctions for catalysis, *Chem. Soc. Rev.* 42 (2013) 6593–6604.

[69] Y.C. Su, Y.C. Hsueh, C.C. Kai, C.T. Lia, T.P. Petag, Fabrication of high-activity hybrid Pt@ZnO catalyst on carbon cloth by atomic layer deposition for photoassisted electro-oxidation of methanol, *J. Phys. Chem. C* 117 (2013) 11610–11618.

[70] N.A.M. Barakat, M. Motlak, A.A. Elzatahry, K.A. Khalil, E.A.M. Abdelghani, Ni<sub>x</sub>Co<sub>1-x</sub> alloy nanoparticle-doped carbon nanofibers as effective non-precious catalyst for ethanol oxidation, *Int. J. Hydrogen Energy* 39 (2014) 305–316.

[71] S. Pylypenko, E.J. Peterson, B. Halevi, E. Champagne, T.S. Olson, P. Atanassov, Hierarchically structured Pt–alloy ethanol oxidation electrocatalysts, *Electrocatalysis* 3 (2012) 334–345.

[72] J.V. Perales-Rondon, J. Solla-Gullon, E. Herrero, C.M. Sanchez-Sanchez, Enhanced catalytic activity and stability for the electrooxidation of formic acid on lead modified shape controlled platinum nanoparticles, *Appl. Catal. B: Environ.* 201 (2017) 48–57.

[73] S.S. Mahapatra, J. Datta, Characterization of Pt–Pd/C electrocatalyst for methanol oxidation in alkaline medium, *Int. J. Electrochemistry* 2011 (2011) 563495.